Article

Electroporation of Brain Endothelial Cells on Chip toward Permeabilizing the Blood-Brain Barrier

Mohammad Bonakdar,[1,*] Elisa M. Wasson,[1] Yong W. Lee,[2,3] and Rafael V. Davalos[1,2,3]

[1]Department of Mechanical Engineering and [2]Department of Biomedical Engineering and Mechanics, Virginia Tech, Blacksburg, Virginia; and [3]School of Biomedical Engineering and Sciences, Virginia Tech – Wake Forest University, Virginia Tech, Blacksburg, Virginia

ABSTRACT   The blood-brain barrier, mainly composed of brain microvascular endothelial cells, poses an obstacle to drug delivery to the brain. Controlled permeabilization of the constituent brain endothelial cells can result in overcoming this barrier and increasing transcellular transport across it. Electroporation is a biophysical phenomenon that has shown potential in permeabilizing and overcoming this barrier. In this study we developed a microengineered in vitro model to characterize the permeabilization of adhered brain endothelial cells to large molecules in response to applied pulsed electric fields. We found the distribution of affected cells by reversible and irreversible electroporation, and quantified the uptaken amount of naturally impermeable molecules into the cells as a result of applied pulse magnitude and number of pulses. We achieved 81 $\pm$ 1.7% ($N = 6$) electroporated cells with 17 $\pm$ 8% ($N = 5$) cell death using an electric-field magnitude of ~580 V/cm and 10 pulses. Our results provide the proper range for applied electric-field intensity and number of pulses for safe permeabilization without significantly compromising cell viability. Our results demonstrate that it is possible to permeabilize the endothelial cells of the BBB in a controlled manner, therefore lending to the feasibility of using pulsed electric fields to increase drug transport across the BBB through the transcellular pathway.

INTRODUCTION

Many potential therapeutics for disorders of the central nervous system (CNS), which are proven to be effective in vitro, have limited to no effect in vivo. This is due to their large molecular weight, water solubility, and charge, which render it difficult for them to successfully cross the blood-brain barrier (BBB). Only small and lipid-soluble molecules are able to passively cross the BBB, therefore protecting the brain from harmful invading pathogens. Despite its protecting nature, most drugs used to treat CNS disorders are large water-soluble molecules, therefore making the BBB a significant hindrance in treating patients. In the United States alone, 80,000,000 people are suffering from CNS disorders such as brain cancer, Alzheimer's, and Parkinson's disease (1). Despite the high need for development of effective CNS drugs, only a small portion of newly discovered therapeutics have been found to be clinically relevant and have the ability to overcome the BBB.

The BBB is comprised of a layer of highly restrictive cells that line the walls of brain microvessels. Different vascular and parenchymal cell types contribute to the formation of this barrier including endothelial cells, astrocytes (2), pericytes (3), neurons, the extracellular matrix, and the basement membrane (4,5). Despite containing various cell types, 75–80% of the contribution to barrier function is made by the brain capillary endothelial cells lining the luminal surface of the microvessels (6). These endothelial cells form intercellular tight junctions (TJs), which limit the transport of hydrophilic molecules larger than 500 Da (7). Therefore, the biggest obstacle in delivering an effective treatment to brain tissue is penetrating this endothelial cell layer. Normal and disrupted transport across this layer may occur through two pathways: the transcellular pathway, which is through the cell membrane and cytosol; and the paracellular pathway, which is located at the cell-cell TJs.

Many researchers have proposed different techniques to temporarily bypass or permeabilize the BBB through these pathways. These include focused ultrasound (8,9), osmotic disruption (10), drug delivery vehicles (11,12), and pulsed electric fields (PEFs) (13,14) including electroporation (15,16). All of these techniques have inherent advantages and drawbacks. Despite showing the capability to noninvasively and reversibly disrupt the BBB, focused ultrasound is limited by the small coverage area the focal beam can target, leading to extended treatment times for large tissue volumes (17). Osmotic and pharmacological disruption using agents such as mannitol or bradykinin have also been studied as a way to transiently open the BBB, but have been found to do so in a systemic manner that may lead to adverse effects such as headache, nausea, and abnormal neuron function (9,18). In addition, researchers have shown immunoliposomes, endogenous peptides, or other vehicles successfully carry therapeutic drugs across the BBB (19,20). Once there,

---

many are unable to reach the concentration necessary for effective treatment.

Alternatively, PEFs have shown promise in treating neurological and psychiatric disorders. PEFs are short, intense electrical pulses that have been used in deep brain stimulation (21,22), electrochemotherapy (23,24), and irreversible electroporation (IRE) (25–27) for tumor ablation. Electroporation is a biophysical phenomenon in which PEFs applied across a cell cause the transmembrane potential to exceed a certain threshold value, thus creating pores in the membrane (28). Electroporation can be either reversible (where pores reseal over time), or irreversible (where pores grow too large to recover, according to the pulse parameters applied (29,30)). Irreversible electroporation results in cell death due to the induced permanent defects in the cell membrane. However, even when the cell membrane eventually recovers, the phenomenon may apoptotically result in cell death due to the induced chemical imbalance in the cell during the electroporation period (31). While irreversible electroporation may nonthermally ablate tissues (25), reversible electroporation may be used in a controlled manner to temporarily disrupt the cell membrane for gene or drug delivery (32). In the paracellular pathway, TJs significantly restrict transport in between cells due to their secure connection to the cytoskeleton. Because PEFs disrupt the cell membrane, and therefore the cytoskeleton, they have the potential to disrupt the TJs as well (13). This indicates that PEFs have the potential to enhance permeability of either the transcellular or the paracellular pathways of the BBB. In brain capillary cells, transcytosis of macromolecules is also extremely limited due to the low amount of caveolae (33). Caveolae are lipid rafts that selectively internalize molecules at the plasma membrane. According to the literature, one form of transcellular transport is passive diffusion through the lipid bilayer and the cytoplasm from the luminal to the abluminal side of the BBB (7). Because electroporation disrupts the lipid bilayer, it is concluded that it could potentially reduce the inherent resistance to passive diffusion across the transcellular pathway and increase the transcellular permeability of the BBB. To our knowledge, the distinction between permeabilization of different pathways across the BBB has rarely been studied in the literature.

Several studies have explored the effects of PEFs on the integrity of the BBB. Lopez-Quintero et al. (13) probed deep-brain-stimulation-relevant waveforms and intensities on the permeability of the BBB using an in vitro setup. They found that the water flux across the endothelial cell layer is increased by applying high frequency PEFs of up to 185 Hz and 2.50 V/cm magnitude. Garcia et al. (15) investigated the effects of low intensity EF on BBB transport in an in vivo study. They found that the threshold for BBB disruption is between 400 and 600 V/cm for ninety 50-μs pulses delivered at 1 Hz. In another in vivo study, Arena et al. (14) studied the effect of bipolar submicrosec-

ond pulses on BBB permeability and found that BBB disruption occurs at much lower thresholds of 250 V/cm without any muscle contraction. Hjouj et al. (16) studied reversible and irreversible electroporation thresholds of the BBB in rats and monitored the disruption by magnetic resonance imaging. They found that reversible disruption occurred between EF intensities of 330 V/cm and 500 V/cm using a total number of 50–70 μs pulses at a frequency of 4 Hz, resulting in BBB disruption volumes larger than tissue damage volumes. Other experimental studies have also investigated the effect of electroporation on the permeability of endothelial cells in vitro (34) and in vivo (35), with a focus on the paracellular pathway.

In vivo experiments on BBB permeabilization, such as the ones mentioned above, provide mostly qualitative results, therefore making in vitro models necessary for obtaining more quantitative analysis; however, their physiological relevance is always a matter of debate. Several in vitro models have been previously developed to simulate the integrity and permeability of the BBB to different substances (36,37) as well as investigate the effect of different stimuli such as chemicals (38), pressure shock (39), radiation (40), and electromagnetic fields (41–43). Microfluidics studies provide an alternative platform to standard in vitro systems for analyzing cells and tissues in a more physiologically relevant environment (44,45). Organs-on-chip platforms utilize the advantages of microfluidics to recreate in vivo conditions of the body in an easily testable, in vitro setting. Several investigators have developed dynamic models of the BBB by culturing brain endothelial cells inside microfluidic channels (46–49) and investigating permeability of the BBB to different therapeutics.

While these in vivo and in vitro studies have provided insight into the permeability of the BBB in response to PEFs and other therapeutics, no distinction has been made between the paracellular and transcellular pathways. Although both of these pathways are essential in transporting molecules across the BBB, each of them allow for quite specific, distinct molecules to cross depending on their size and hydrophilic or hydrophobic nature. Therefore the ability to target and controllably permeabilize each independently may allow for better delivery of drugs.

As previously mentioned, the transcellular pathway includes the cell membrane, the cytoplasm, and again the cell membrane. For transcellular transport to occur, molecules are first uptaken through the luminal side of the cell membrane into the cytoplasm, and then pass through to the abluminal side of the membrane. In this work we studied the diffusion process by tracking the molecules during half of their complete transcellular transport, which is from the luminal side to the cytosol of the endothelial cells. Monitoring cellular uptake can give insight into possible enhancement of transcellular transport of different substances.

In this work we expanded on previous in vitro electroporation studies, which were mostly conducted on suspended cells, by quantifying the uptaken amount of molecules in response to applied PEFs. The results from varying pulse strength and number of applied pulses may provide information that can be used to find the proper parameters for the possible enhancement of transcellular transport across the BBB using PEFs without causing any permanent damage.

MATERIALS AND METHODS

Device design and fabrication

The microfluidic channel used in these studies consisted of a nonlinearly tapered geometry, 30 mm long and varying in width, ranging from 1000 μm at the ends to 300 μm at the center. Applying an electric potential to the ends of the channel created a gradient of electric-field (EF) magnitude inside the channel and over the cells. According to Ohm's law, the EF magnitude inside the channel is governed by

$$E(x) = \frac{1}{\sigma}J(x) = \frac{I}{\sigma A(x)}, \tag{1}$$

where σ is the conductivity of the medium, J is the current density, x is the length along the channel, and A is the cross-sectional area of the channel. It was desired to have a linear gradient of EF along the length of the channel to easily correlate these values with the results obtained from experiments. According to Eq. 1 the magnitude of the EF and the cross section of the channel are inversely proportional. Hence, for $E(x)$ to be linear, the cross-sectional area of the channel needed to be inversely proportional to the length along the channel, x. That requires the channel-width profile to be a section of the curve defined by the $w(x) = (C/x)$ curve, where C is a constant and the endpoints of the section are the values of the desired channel widths, which are 1000 and 300. These endpoints and the constant C are determined by satisfying the boundary conditions

$$w(x) = \frac{C}{x}$$
$$\begin{cases} w(a) = 1000 \\ w(a + 15{,}000) = 300, \end{cases} \tag{2}$$

where a is the x axis value of the curve that gives us a width of 1000. Solving the above equations simultaneously gives the numeric values for a and C. To have a symmetric channel geometry, two of the above sections were attached end-to-end, as shown in Fig. 1 A.

Due to this geometry, the cells in the middle of the channel experienced an EF magnitude 3.3 times greater than the cells at the ends. Designing the device in this manner ensured that each part of the channel showed cell behavior in response to a specific EF magnitude. This gradient design allowed for testing multiple conditions in one experiment. The symmetry of the dual tapered channel also transitioned the high EF region from the channel end (found in a single tapered channel) to its middle, where, due to the ports, there is no disruption of the induced EF. Moreover, the symmetry of the channel mandated a symmetric response from the cells in the channel after exposure to PEFs, which served as a verification tool for each experiment. Finite element analysis was used to verify the magnitude of the EF at each point along the channel. The analysis was performed in COMSOL Multiphysics (Stockholm, Sweden) 4.4 in a two-dimensional model using the AC/DC module. Boundary conditions were defined by a ground potential of 0 V applied to one end of the channel (inlet) and a charged potential corresponding to the pulse magnitude applied to the other end (outlet).
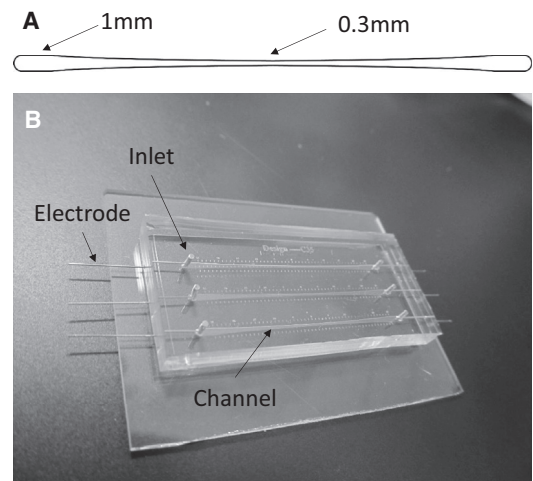
FIGURE 1 (*A*) Tapered channel. (*B*) Microfluidic device comprising three separate dual tapered channels.

Standard photolithography was used to create a silicon mold and subsequently replication molding was used to fabricate the microfluidic channel in PDMS (polydimethylsiloxane) (50) (Sylgard 184; Dow Corning, Waltham, MA). PDMS was prepared by mixing the prepolymer and curing agent with a 10:1 weight ratio. The mixture was then degassed and poured onto the Si wafer. The PDMS was cured at 100°C for 1 h. After curing, the inlets and outlets were punched and the PDMS device was bonded to a glass slide using air plasma (Harrick Plasma, Ithaca, NY). Stainless-steel needles were placed at the inlet and outlet to deliver the pulses. Fig. 1 B shows the fabricated device.

Cell culture

Previous in vitro models of the BBB have been developed from a variety of different primary cells and immortalized cell lines (51). In this study we used the mouse brain endothelial cell line, bEnd.3 (ATCC, Manassas, VA), which has been shown to adequately represent the BBB (6). The bEnd.3 cells were cultured in T-75 flasks at 37°C and 5% CO_2 and maintained in complete growth media consisting of DMEM (ATCC) supplemented with 10% (v/v) fetal bovine serum (Atlanta Biologicals, Flowery Branch, GA) and 1% (v/v) penicillin-streptomycin (Life Technologies, Thermo Fisher Scientific, Waltham, MA). The cells were routinely passaged at 70–90% confluence. To prepare the microfluidic device for cell seeding, the PDMS channels were first sterilized with ethanol. To promote cell adhesion and proliferation, the channel was treated with 50 μg/mL human fibronectin (Trevigen, Gaithersburg, MD) for 1 h in an incubator. Complete growth media was then introduced into the device and incubated for 2 h. Endothelial cells were collected by washing and detaching with trypsin. The trypsin was then neutralized by the addition of media and centrifuged for 5 min at 120 × g. The trypsin solution was removed and fresh media was added to obtain a concentration of ~40,000,000 cells/mL. The cells were then introduced into the device through manual injection using a syringe and tubing until an even distribution was achieved in the channel. The device was incubated at 37°C for 2 h, allowing the cells to fully attach. Then, complete media was provided to the channel using media-filled pipet tips at the inlet and outlet. The devices were incubated for two days at 37°C and 5% CO_2 until the cells were confluent in the channel.

Electroporation

A BTX pulse generator (Harvard Apparatus, Holliston, MA) was used to apply PEFs to the microchannels. The pulse width and frequency were

set at 100 μs and 1 Hz, respectively, which is consistent with clinical electroporation procedures (26). Pulse magnitude was set to 1500 V across the channel for all experiments, which provides relevant EF magnitudes inside the channel ranging from 214 to 714 V/cm. The number of pulses was varied at 10, 30, and 90 to represent both standard electrochemotherapy and IRE procedures and conditions between the two. To find the reversible and irreversible electroporation thresholds, the cellular uptake of propidium iodide (PI) (Life Technologies) both during and after application of PEFs was monitored. PI has been previously used as a permeabilization tracer during electroporation (52). In this study the choice of PI was based on its molecular mass of 668 Da, which is comparable to several CNS drugs listed in the Results and Discussion. To determine the threshold for the onset of cellular uptake during electroporation, a solution of PI in PBS was used as the electroporation buffer and injected into the channel immediately before pulsing. While naturally impermeable, PI stains the cell nuclei when the membrane is compromised. Therefore after pulsing and disrupting the cell membrane, the PI molecules were able to enter the cell and bind to DNA, allowing visualization of the affected cells. To determine the IRE threshold, the cells were pulsed and then allowed to recover for 1 h. Small pores usually recover within a fraction of a second; however, full recovery of larger pores may take longer (53). After recovery, the cells were exposed to the PI solution. In this case, only the permanently damaged cells were affected by PI, allowing visualization and quantification of the IRE phenomenon. In both cases, NucBlue (Life Technologies) was used to counterstain the nuclei and count the total number of cells. The uptake of 4 kDa FITC-dextran (Sigma-Aldrich, St. Louis, MO) as a result of applying PEFs was also investigated. In these experiments, the channels were filled with a solution of the substance (10 mg/mL in PBS) before pulsing. After the pulsing is completed, the channel is rinsed with media for five minutes to remove the FITC-dextran from the channel. That would restrict the fluorescence to the cells and eliminate background light. The cells are then visualized with fluorescent microscopy to quantify uptake.

Fluorescent microscopy and image processing

Fluorescent images were taken of the cells in the channel using an inverted microscope (Carl Zeiss, Jena, Germany) equipped with a CoolSNAP HQ2 CCD camera (Photometrics, Tucson, AZ) and automated stage. The microscope was controlled using the ZEN Pro 2012 software (Carl Zeiss). The tiling feature of the software was used to image the entire length of the channel. To enhance the contrast and brightness of the images and to remove background noise, images were processed in ImageJ (NIH, Bethesda, MD). The intensity was then acquired along the channel and normalized to the width of the channel. The normalized fluorescence intensity was used as a quantitative measure of uptaken molecules as explained in the following sections. To calculate the percentage of dead cells, the fluorescent light intensities from PI (red) and NucBlue (blue) were adjusted in ImageJ to restrict the light to the cell nuclei. This causes the light intensity from each portion of the channel to be proportional to the number of cells. The percentage of dead cells was obtained by dividing the intensity of the dead cells (red) to that of the total cells (red+blue) in each 3-mm section along the channel.

Confocal microscopy

Confocal microscopy was performed to obtain the average height of the cell monolayer to develop the calibration curve used to quantify cellular uptake of dextran. Before imaging, the cells were fixed with 4% paraformaldehyde (Boston BioProducts, Ashland, MA) and stained with rhodamine phalloidin and DAPI (Invitrogen, Carlsbad, CA), used to stain F-actin filaments and nuclei, respectively. After staining, the cells in the microchannel were imaged using a LSM880 confocal microscope (Carl Zeiss) with a 40× objective. The pinhole aperture for confocal fluorescence was adjusted to produce a Z resolution of ~1 μm. Images were collected in steps of
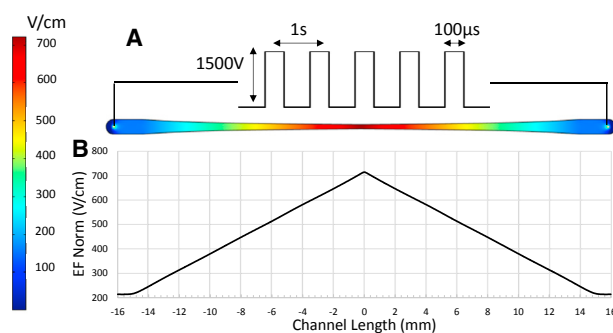
FIGURE 2 EF distribution in the channel as a result of applied potential at the channel ends. (A) EF contours in the channel and (B) EF magnitude along the channel centerline. To see this figure in color, go online.

0.1 μm in the Z direction. ZEN Black software (Carl Zeiss) was used to analyze the sections and build the three-dimensional image.

Fluorescent calibration

To relate the fluorescence intensity of the images to the concentration of the uptaken dextran molecules, a calibration curve was developed. This was done by using microfluidic channels of different heights to simulate the height of the adhered cells found using confocal microscopy. The channels were filled with solutions of different concentrations of 4 kDa FITC-dextran in PBS and imaged. The fluorescence intensity was then obtained using ImageJ (National Institutes of Health).

Statistical analysis

Statistical analyses were performed using JMP Pro, ver. 11.0 (SAS Institute, Cary, NC) with a confidence level of $\alpha = 0.05$. Two-way analysis of variance (ANOVA) was used to test for differences in the number of dead cells after IRE treatment ($N = 5$) as well as the cellular uptake of PI ($N = 6$) and dextran ($N = 3$). When results of ANOVA were significant, Tukey post hoc comparisons were used to examine differences among treatment groups. Data are presented as arithmetic mean $\pm$ SD.

RESULTS AND DISCUSSION

EF distribution inside the channel using finite element analysis

Fig. 2 shows the EF distribution in the channel and the EF magnitude along the centerline of the channel for an applied potential of 1500 V. As shown in the figure, the design of the channel provided a linear variation in the EF magnitude from 213 V/cm at the ends to 714 V/cm at the center of the channel. It should also be noted that the EF magnitude did not change significantly along the width of the channel.

Calibration of fluorescent intensity for different heights in terms of the concentration of fluorescent molecules

Fig. 3 shows the fluorescent intensity as a function of the concentration of 4 kDa FITC-dextran inside channels of different heights. Our observations using confocal
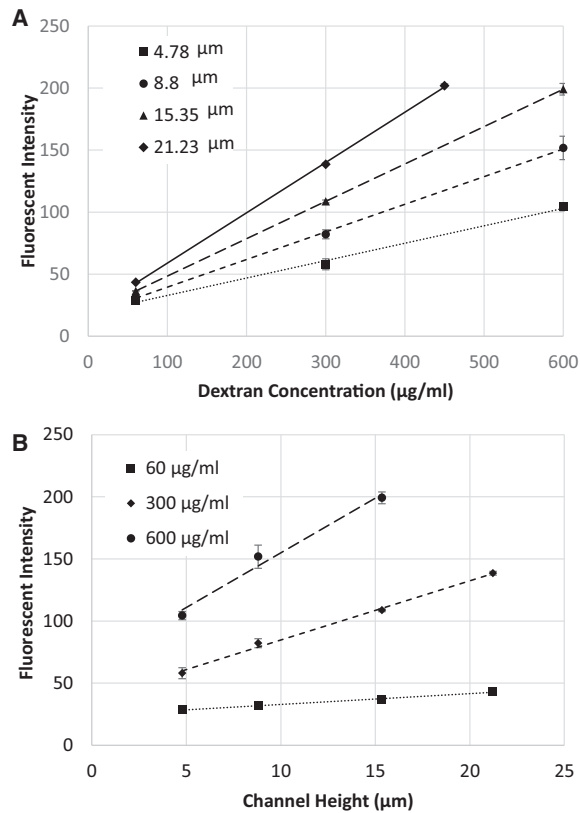
FIGURE 3 Calibration curves for fluorescent intensity of 4 kDa FITC dextran in the microchannel: (*A*) for different heights; (*B*) for different concentrations.

microscopy showed that after adhesion and spreading, the thickness of the cell monolayer varied between 2 μm (at the cell edges) to ~7 μm (above the nuclei). Hence, four different heights around this range were selected for obtaining the calibration curves. It was found that the intensity varied linearly with respect to both the concentration and the height. Linear regression was used to find an empirical relation giving the fluorescence intensity as a function of FITC-dextran concentration and height. The linear dependence of intensity on channel height was used in the following section to obtain the profile of adhered endothelial cells according to the fluorescence of absorbed dextran.

Characterization of the cell monolayer height inside the microchannel

Fig. 4 shows cross-sectional images of the cell monolayer at different heights from the channel base, as well as several side views of the cells along different transverse sections. The maximum height of the cells was located above the cell nuclei with an average value of 7.0 $\pm$ 1.4 μm. The rest of the cell body possessed a maximum height of <4 μm. The staining technique clearly visualized the boundary of the nucleus, but not the boundary of the cell body, as shown in the side views of Fig. 4. Despite a sharply

contrasted nucleus, the rest of the cell body was blurred. Hence another technique using the fluorescent intensity of uptaken FITC-dextran was used to find the outer profile of adhered cells. Based on the size of the cells and the diffusivity of the dextran molecules inside the cytosol, it is possible to assume a uniform distribution of absorbed dextran in the cell body after a few minutes. Therefore, the fluorescent intensity at each point becomes linearly proportional to the height of the adhered cell, as shown in the calibration section (Fig. 3 *B*). We used this fact in addition to the absolute height of the cells above the nuclei—according to the confocal imaging—to find the height distribution of the adhered cells.

Fig. 5 shows the adhered bEnd.3 cells in the microchannel and the outer profile along their longitudinal directions. Using this method, the average height of the endothelial cell monolayer was calculated to be 3.15 μm ($N = 30$).

Determination of the reversible and irreversible electroporation thresholds

When using PEFs to permeabilize the endothelial cells of the BBB for drug transport, it is desirable to avoid irreversible effects on the cell membrane, which can result in permanent damage and leakage of the blood vessels. Hence, it is necessary to know the IRE threshold and the margin for reversible electroporation. The IRE threshold is a function of an applied number of pulses. A treatment comprising more pulses needs a lower EF magnitude to induce IRE. Fig. 6 shows the distribution of dead cells inside the channel for different numbers of pulses. (See Fig. S1 in the Supporting Material for a high-resolution image of the electroporated cells in the channel.) As shown, by increasing the number of pulses, more cells in the lower EF region (wider section of the channel) were irreversibly electroporated. Expanding upon this, Fig. 7 shows the percentage of dead cells along the channel for different numbers of pulses and pulse magnitudes. It should be noted that no chemical reaction or bubbling was observed around the pulsing electrodes inside the channel, which is mainly attributed to the small pulse width (100 μs) and low current (~2 mA).

Factors such as cell orientation (54), cell size, and distribution density (55) cause individual cells to be affected differently by the pulses of the same magnitude. Our experiments showed that the cells that are oriented parallel to the electric field get electroporated at a lower electric field than those that are perpendicular to the field. (See Movie S1 for time-lapse videos of cells during electroporation.) Previous modeling for spheroidal cells has proven the same behavior (54). This results in a distribution of live/dead cells along the channel instead of a sharp delineation between live and dead cells. The percentage of dead cells differed significantly among the examined treatment parameters (ANOVA, $p <$ 0.0001). Post hoc comparisons indicated that the dead cell percentage for 10 pulses was significantly different from
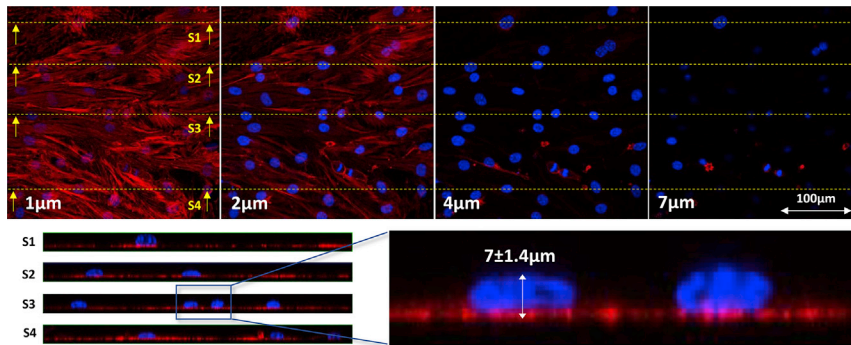
FIGURE 4 Confocal images of the endothelial cell monolayer. (*Top*) Cross-sectional images of the bEnd.3 cell monolayer in the microchannel taken at different heights. (*Bottom*) Side views show the relative height of the nuclei (*blue*) compared to the rest of the cell body (*red*). To see this figure in color, go online.

30 and 90 pulses at higher EF magnitudes whereas lower EF magnitudes (245–314 V/cm) did not show a significant difference. These results can be seen in Fig. 7, which shows that for a wide range of EF magnitude, the induced cell death for 10 pulses (0–40%) is much lower than 30 and 90 pulses (5–100%). This finding is consistent with the fact that usually 8–10 pulses are applied for drug delivery during electrochemotherapy. For 10 pulses, almost no cell death is observed for EF <400 V/cm. It can also be seen that 30 and 90 pulses at higher EF magnitudes (646–714 V/cm) and low EF magnitudes (245 V/cm) did not result in a significantly different percentage of cell death whereas an EF magnitude of 314 V/cm for 30 and 90 pulses resulted in significantly different percentages. Similar in vitro experiments have been conducted by Dermol et al. (56), where pulse number and electric field were varied to determine the influence these parameters have on cell survival and also to evaluate mathematical models of cell survival. The authors tested Chinese hamster ovary cells in suspension with pulse numbers of 8, 30, and 90. Each of these pulses were 100 μs in duration, with the electric field ranging from 500 to 4000 V/cm. It was found that

the majority of cells survived treatments with an electric field of 1000 V/cm with little distinction between different pulse numbers. A difference among 8, 30, and 90 pulses was not seen until the applied electric field reached 2000 V/cm. Therefore the threshold for irreversible electroporation was found to be higher than what was found in our experiments, where close to 100% of cells became irreversibly electroporated at 714 V/cm (Fig. 7). This may be because we are using a different cell type that contains strong intercellular junctions. These junctions as well as cell geometry have been shown to influence transmembrane potential (57), causing results to be different from cells tested in suspension. Previous in vivo studies also show that an EF magnitude of 500 V/cm and 90 pulses induce IRE (16). Our results show that the same pulsing, results in 85% cell death.

Fig. 8 shows the distribution of electroporated cells visualized by uptake of PI. The percentage of electroporated cells differed significantly among the examined treatment parameters (ANOVA, $p < 0.0001$). Post hoc comparisons indicated that the electroporated cell percentage for 10 pulses was significantly different from 30 and 90 pulses at mid-range EF magnitudes (314–513 V/cm), whereas low and high EF magnitudes (245, 646–714 V/cm) did not show a significant difference. Differences between 30 and 90 pulses were not statistically significant for equivalent EF, which indicates that 30 pulses deliver an amount of PI into the cell comparable to 90 pulses. The electroporated cells spanned a wider range of EF compared to the irreversibly electroporated cells. This is because the cells were in contact with the PI molecules during treatment; as soon as the pores opened, the molecules permeated the cells. However, in the case of IRE, only the pores that were not recovered after 1 h allowed the transport of PI molecules into the cell. (Refer to Movie S1 for videos showing the uptake of PI during electroporation.) Dermol and Miklavčič (58) also conducted electroporation experiments on adhered cells after delivering only 1 pulse of 1 ms, and found that the higher the cell density, the lower the percentage of cells that are electroporated. It is difficult to compare our results directly with this study due to the difference in the applied number of pulses. However, our results show that the percentage of electroporated cells is higher than
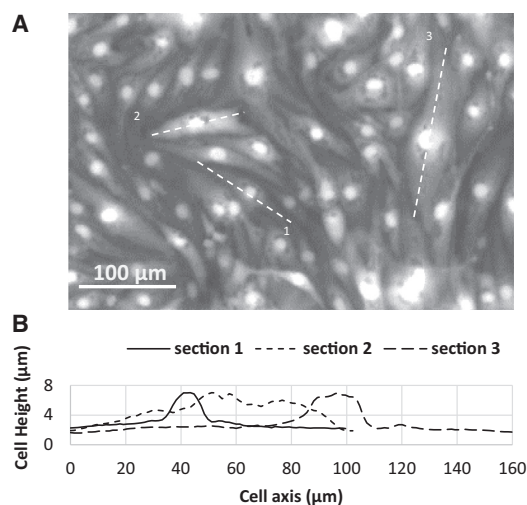

FIGURE 5 Finding the height profile of cells from fluorescent imaging. (*A*) Fluorescence image of adhered bEnd3 cells with absorbed FITC-dextran. (*B*) Height profile of the adhered cells.
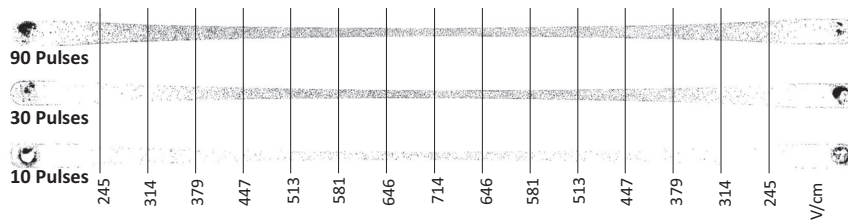
FIGURE 6 Distribution of IRE-treated cells for different numbers of pulses. (See Fig. S1 for high-resolution color image.)

what is found in Dermol and Miklavčič (58). This is because the bEnd3 cells spread out and become very long in the channel, leading to a lower density of cells in the channel than what would be found with Chinese hamster ovary cells. This lower density in turn lowers the electroporation threshold. As previously mentioned, it is also possible that some of the bEnd3 cells were aligned parallel to the electric field, therefore causing them to be electroporated at a lower threshold.

By comparing Figs. 7 and 8, one can find the proper number and magnitude of pulses for cell electroporation with minimal cell death. This comparison is made in Fig. 9 for the specific case of 10 and 90 pulses, which are typically used for electrochemotherapy and tumor ablation treatments, respectively. This comparison demonstrates how different EF magnitudes and pulse numbers can electroporate a population of cells while keeping them viable. It is shown that for 10 pulses, there is a drastic difference between the onset of electroporation and the onset of IRE. For example, 10 pulses at 513 V/cm electroporated ~60% of the cells while causing only 10% cell death. On the other hand for the case of

90 pulses, <20% of the cells that were electroporated remained alive. These results explain the reason eight pulses are typically delivered during electrochemotherapy treatments (59). It should be noted that PI becomes fluorescent once it binds to DNA after entering the cell. Because PI is not intrinsically fluorescent, the emitted light is restricted to the cell nuclei and does not reflect the quantitative amount of PI molecules present in the cell body. To study this uptake phenomenon in a more quantitative manner, the cells were electroporated in the presence of FITC-dextran.

Uptake of large impermeable molecules due to PEFs

Four kiloDaltons of FITC-dextran is intrinsically fluorescent and naturally impermeable to the cells due to its large size and hydrophilic nature. However, this substance can penetrate the cell membrane through induced pores formed by electroporation. Fig. 10 shows the uptake of 4 kDa dextran after electroporation. (For a high-resolution image, refer to Fig. S2.) The percentage of affected cells differed significantly among the examined treatment parameters (ANOVA, $p < 0.0001$). Post hoc comparisons indicated that the uptake of FITC-dextran into cells for 10 pulses was significantly different from 30 and 90 pulses at high EF magnitudes (646–714 V/cm) whereas low EF magnitudes for 30 pulses (245–314 V/cm) and midrange EF for 90 pulses (447–513 V/cm) did not show a significant difference. Differences between 30 and 90 pulses were statistically significant for midrange EF magnitudes (447–581 V/cm). Fig. 11 indicates that uptake of dextran into the cells was more effective for lower EF magnitudes for 30 and 90 pulses, which initially may seem counterintuitive. For cells that were reversibly electroporated, the molecules became trapped inside the cells after the pores were recovered. For the cells that were irreversibly electroporated, it is possible that the membrane remained leaky and could not retain the absorbed molecules for the duration of the experiment. Therefore, we hypothesize that dextran molecules escaped the cells during the 5-min washing period, reducing the emitted fluorescent light from those regions of the channel. This behavior was not observed for the uptake of PI (Fig. 8), because PI binds to the DNA as soon as uptake occurs and cannot exit the cell. Fig. 11 A shows the fluorescent intensity of absorbed 4 kDa dextran along the channel for different numbers of pulses. Knowing the calibration curve for fluorescent intensity and the cell monolayer thickness, it was
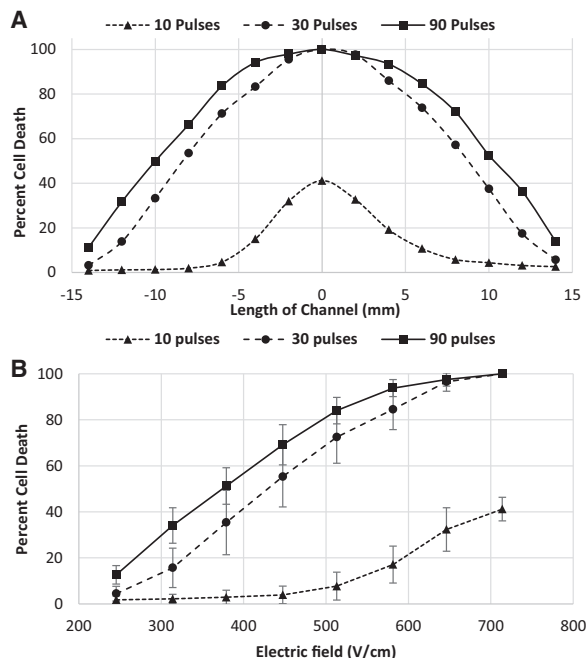

FIGURE 7 Distribution of dead cell population after electroporation. (A) Dead cell population along the channel for different numbers of pulses. (B) Dead cell population as a function of PEF magnitude for different numbers of pulses.
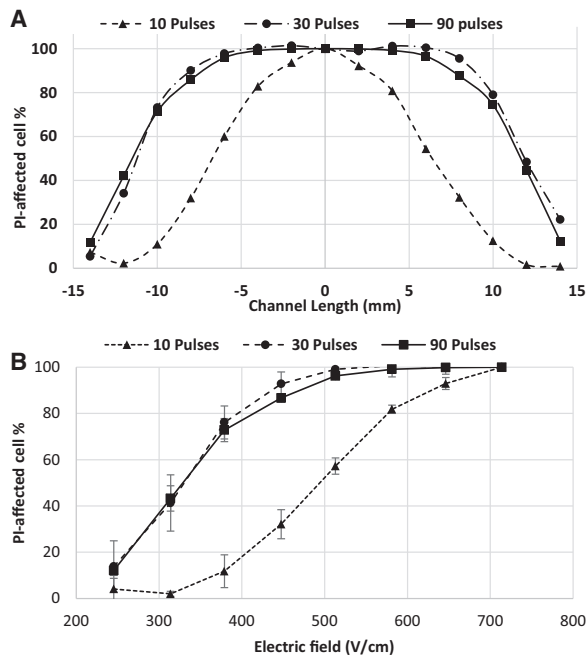
FIGURE 8   Distribution of PI-permeated cells after electroporation. (*A*) PI-permeated cell population along the channel for different numbers of pulses. (*B*) PI-permeated cell population as a function of PEF magnitude.

possible to find the approximate concentration of the accumulated dextran inside the cells. Fig. 11 *B* shows dextran concentration versus EF magnitude for different numbers of pulses. Depending on the applied number of pulses, different ranges of EF magnitude gave maximum uptake of the dextran molecules. For the case of 10 pulses, generally the higher the EF magnitude, the higher the amount of uptake. This is due to the dominant occurrence of reversible electroporation instead of IRE even at the highest EF magnitude of 714 V/cm. In other words, despite some cells dying by increasing the EF magnitude, other cells uptake enough molecules that the overall uptake by the monolayer is seen as increasing. However, that was not the case when the number of applied pulses was increased. Increasing the number of pulses resulted in more cell death at the
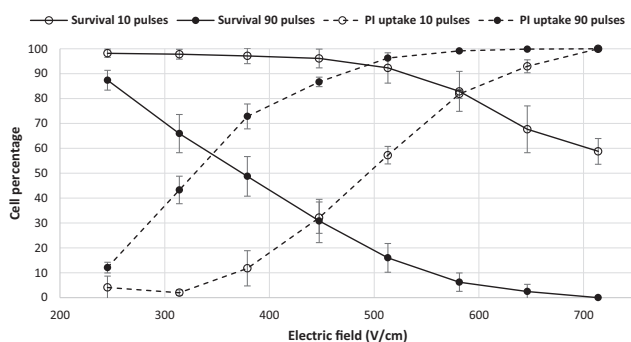
higher EF zone. The maximum uptake for 10 pulses (at 714 V/cm) is higher than the maximum uptake for 30 and 90 pulses (at 447 and 379 V/cm, respectively), because there is a low percentage of dead cells at 10 pulses compared to 30 and 90, as seen in Fig. 7.

It should be noted that in the case of passive diffusion across the intact cell membrane, the transcellular pathway is restricted to lipophilic molecules. However, electroporation can induce hydrophilic pores into the membrane, which may facilitate the transport of hydrophilic molecules such as dextran in this case. In the above experiments, the rationale for choosing PI (668 Da) and FITC-dextran (4 kDa) as the target molecules was their resemblance in size to several drugs, which are currently being administered to patients with brain diseases and tumors for which penetration of the BBB remains a challenge. These drugs include Bleomycin, 1415 Da; Doxorubicin, 543 Da; Amphotericin B, 923 Da; and Paclitaxel, 853 Da. Being slightly larger than these drugs, the results for the uptake of 4 kDa FITC-dextran into brain endothelial cells gives an upper limit for the uptake of these drugs into the BBB by applying the proper PEFs without causing any permanent damage to the BBB.

In addition to reversible electroporation that opens the transcellular pathway for transfer of substances, PEFs may also disrupt the TJs between the adjacent cells that open the paracellular pathway (60). This study was specifically aimed at finding the thresholds for reversible electroporation and cellular uptake of different-sized molecules, which could yield relevant information about the possibility of transcellular transport across the BBB. Studying the actual permeability coefficients for paracellular and transcellular pathways requires access to both luminal and abluminal sides of the BBB, which is left for future studies.

CONCLUSION

In this study we quantified the uptaken amount of molecules into adhered brain endothelial cells as a function of 1) EF magnitude and 2) the number of pulses by using emitted fluorescent light from the electroporated cells. To the best of our knowledge, it is the first time that such analysis has been performed for electroporated cells. We implemented a tapered microfluidic channel to apply a gradient of EF on adhered brain endothelial cells and visualized the electroporation phenomenon by tracking the uptake of different naturally impermeable molecules into the cells. The tapered design allowed for testing of multiple conditions in one experiment, therefore making it a useful platform to test drug delivery using PEFs. Using this platform, we were able to show the difference between reversible and irreversible electroporation for different pulse numbers and a wide range of EF magnitudes. The majority of the cells that were electroporated with 10 pulses recovered; however, electroporation with 30 and 90 pulses was

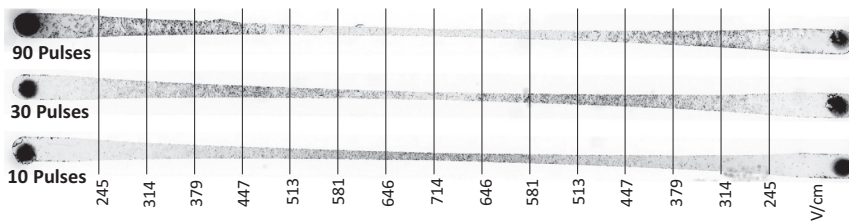FIGURE 9   Comparison of IRE and PI uptake for 10 and 90 pulses.

FIGURE 10 Uptake of 4 kDa FITC-dextran for different numbers of pulses. (See Fig. S2 for a high-resolution image.)

mostly irreversible. Results for 30 and 90 pulses were similar for the entire range of EF magnitude, although 90 pulses caused more cell death. These results provide the proper range of applied EF magnitude and number of pulses for safe permeabilization without significantly compromising cell viability. Our results demonstrate that it is possible to permeabilize the endothelial cells of the BBB in a controlled manner, adding to the feasibility of using PEFs to increase drug transport across the BBB via the transcellular pathway.

SUPPORTING MATERIAL

Two figures and one movie are available at http://www.biophysj.org/biophysj/supplemental/S0006-3495(15)04701-3.
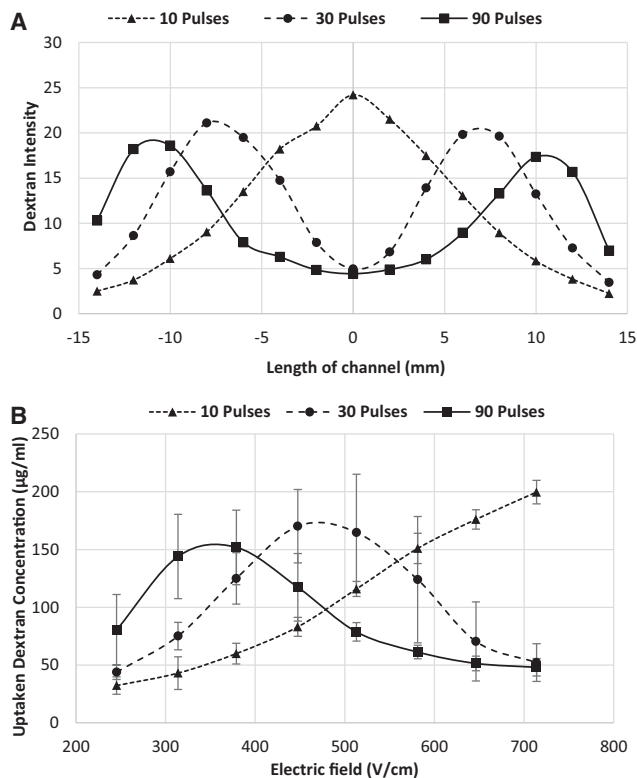

FIGURE 11 Dextran uptake during electroporation. (*A*) Fluorescent intensity along the channel for different numbers of pulses. (*B*) Dextran concentration inside cell after pulsing versus EF for different numbers of pulses. The dextran concentration in the pulsing medium was 10 mg/mL. (Refer to the Supporting Material for a high-resolution image of dextran uptake into the cells within the channel.)

REFERENCES

1. Pardridge, W. M. 2002. Why is the global CNS pharmaceutical market so under-penetrated? *Drug Discov. Today.* 7:5–7.

2. Abbott, N. J., L. Rönnbäck, and E. Hansson. 2006. Astrocyte-endothelial interactions at the blood-brain barrier. *Nat. Rev. Neurosci.* 7:41–53.

3. Lai, C. H., and K. H. Kuo. 2005. The critical component to establish in vitro BBB model: pericyte. *Brain Res. Brain Res. Rev.* 50:258–265.

4. Hawkins, B. T., and T. P. Davis. 2005. The blood-brain barrier/neurovascular unit in health and disease. *Pharmacol. Rev.* 57:173–185.

5. Chen, Y., and L. Liu. 2012. Modern methods for delivery of drugs across the blood-brain barrier. *Adv. Drug Deliv. Rev.* 64:640–665.

6. Li, G., M. J. Simon, …, B. M. Fu. 2010. Permeability of endothelial and astrocyte co-cultures: in vitro blood-brain barrier models for drug delivery studies. *Ann. Biomed. Eng.* 38:2499–2511.

7. Fu, B. M. 2012. Experimental methods and transport models for drug delivery across the blood-brain barrier. *Curr. Pharm. Biotechnol.* 13:1346–1359.

8. Hynynen, K., N. McDannold, …, N. Vykhodtseva. 2005. Local and reversible blood-brain barrier disruption by noninvasive focused ultrasound at frequencies suitable for trans-skull sonications. *Neuroimage.* 24:12–20.

9. Treat, L. H., N. McDannold, …, K. Hynynen. 2007. Targeted delivery of doxorubicin to the rat brain at therapeutic levels using MRI-guided focused ultrasound. *Int. J. Cancer.* 121:901–907.

10. Kroll, R. A., and E. A. Neuwelt. 1998. Outwitting the blood-brain barrier for therapeutic purposes: osmotic opening and other means. *Neurosurgery.* 42:1083–1100.

11. Unger, E. C., T. Porter, …, R. Zutshi. 2004. Therapeutic applications of lipid-coated microbubbles. *Adv. Drug Deliv. Rev.* 56:1291–1314.

12. Pardridge, W. M. 2002. Drug and gene targeting to the brain with molecular Trojan horses. *Nat. Rev. Drug Discov.* 1:131–139.

13. Lopez-Quintero, S. V., A. Datta, …, J. M. Tarbell. 2010. DBS-relevant electric fields increase hydraulic conductivity of in vitro endothelial monolayers. *J. Neural Eng.* 7:16005.

14. Arena, C. B., P. A. Garcia, ..., R. V. Davalos. 2014. Focal blood-brain-barrier disruption with high-frequency pulsed electric fields. *Technology (Singap.).* 2:206–213.

15. Garcia, P. A., J. H. Rossmeisl, Jr., ..., R. V. Davalos. 2012. 7.0-T magnetic resonance imaging characterization of acute blood-brain-barrier disruption achieved with intracranial irreversible electroporation. *PLoS One.* 7:e50482.

16. Hjouj, M., D. Last, ..., Y. Mardor. 2012. MRI study on reversible and irreversible electroporation induced blood brain barrier disruption. *PLoS One.* 7:e42817.

17. Liu, H.-L., M.-Y. Hua, ..., K.-C. Wei. 2010. Blood-brain barrier disruption with focused ultrasound enhances delivery of chemotherapeutic drugs for glioblastoma treatment. *Radiology.* 255:415–425.

18. Warren, K., R. Jakacki, ..., F. M. Balis. 2006. Phase II trial of intravenous lobradimil and carboplatin in childhood brain tumors: a report from the Children's Oncology Group. *Cancer Chemother. Pharmacol.* 58:343–347.

19. Prokai-Tatrai, K., L. Prokai, and N. Bodor. 1996. Brain-targeted delivery of a leucine-encephalin analogue by retrometabolic design. *J. Med. Chem.* 39:4775–4782.

20. Huwyler, J., D. Wu, and W. M. Pardridge. 1996. Brain drug delivery of small molecules using immunoliposomes. *Proc. Natl. Acad. Sci. USA.* 93:14164–14169.

21. Agnesi, F., M. D. Johnson, and J. L. Vitek. 2013. Chapter 4. Deep brain stimulation: how does it work? *In* Handbook of Clinical Neurology. M. L. Andres and H. Mark, editors. Elsevier, New York, pp. 39–54.

22. Sandyk, R. 1997. Treatment with electromagnetic fields reverses the long-term clinical course of a patient with chronic progressive multiple sclerosis. *Int. J. Neurosci.* 90:177–185.

23. Salford, L. G., B. R. R. Persson, ..., L. M. Mir. 1993. A new brain tumour therapy combining bleomycin with in vivo electropermeabilization. *Biochem. Biophys. Res. Commun.* 194:938–943.

24. Agerholm-Larsen, B., H. K. Iversen, ..., J. Gehl. 2011. Preclinical validation of electrochemotherapy as an effective treatment for brain tumors. *Cancer Res.* 71:3753–3762.

25. Davalos, R. V., I. L. Mir, and B. Rubinsky. 2005. Tissue ablation with irreversible electroporation. *Ann. Biomed. Eng.* 33:223–231.

26. Garcia, P. A., T. Pancotto, ..., R. V. Davalos. 2011. Non-thermal irreversible electroporation (N-TIRE) and adjuvant fractionated radiotherapeutic multimodal therapy for intracranial malignant glioma in a canine patient. *Technol. Cancer Res. Treat.* 10:73–83.

27. Chunlan, J., R. V. Davalos, and J. C. Bischof. 2015. A review of basic to clinical studies of irreversible electroporation therapy. *Biomed. Eng. IEEE Trans.* 62:4–20.

28. Kotnik, T., G. Pucihar, and D. Miklavcic. 2010. Induced transmembrane voltage and its correlation with electroporation-mediated molecular transport. *J. Membr. Biol.* 236:3–13.

29. Rubinsky, B. 2007. Irreversible electroporation in medicine. *Technol. Cancer Res. Treat.* 6:255–260.

30. Orlowski, S., and L. M. Mir. 1993. Cell electropermeabilization: a new tool for biochemical and pharmacological studies. *Biochim. Biophys. Acta.* 1154:51–63.

31. Piñero, J., M. López-Baena, ..., F. Cortés. 1997. Apoptotic and necrotic cell death are both induced by electroporation in HL60 human promyeloid leukaemia cells. *Apoptosis.* 2:330–336.

32. Somiari, S., J. Glasspool-Malone, ..., R. W. Malone. 2000. Theory and in vivo application of electroporative gene delivery. *Mol. Ther.* 2:178–187.

33. Tuma, P., and A. L. Hubbard. 2003. Transcytosis: crossing cellular barriers. *Physiol. Rev.* 83:871–932.

34. Kanthou, C., S. Kranjc, ..., M. Cemazar. 2006. The endothelial cytoskeleton as a target of electroporation-based therapies. *Mol. Cancer Ther.* 5:3145–3152.

35. Corovic, S., B. Markelc, ..., T. Jarm. 2015. Modeling of microvascular permeability changes after electroporation. *PLoS One.* 10:e0121370.

36. Wilhelm, I., C. Fazakas, and I. A. Krizbai. 2011. In vitro models of the blood-brain barrier. *Acta Neurobiol. Exp. (Warsz.).* 71:113–128.

37. Eddy, E. P., B. E. Maleef, ..., P. L. Smith. 1997. In vitro models to predict blood brain barrier permeability. *Adv. Drug Deliv. Rev.* 23:185–198.

38. Franke, H., H.-J. Galla, and C. T. Beuckmann. 1999. An improved low-permeability in vitro-model of the blood-brain barrier: transport studies on retinoids, sucrose, haloperidol, caffeine and mannitol. *Brain Res.* 818:65–71.

39. Hue, C. D., S. Cao, ..., B. Morrison, 3rd. 2013. Blood-brain barrier dysfunction after primary blast injury in vitro. *J. Neurotrauma.* 30:1652–1663.

40. Fauquette, W., C. Amourette, ..., M. Diserbo. 2012. Radiation-induced blood-brain barrier damages: an in vitro study. *Brain Res.* 1433:114–126.

41. Schirmacher, A., S. Winters, ..., F. Stögbauer. 2000. Electromagnetic fields (1.8 GHz) increase the permeability to sucrose of the blood-brain barrier in vitro. *Bioelectromagnetics.* 21:338–345.

42. Franke, H., J. Streckert, ..., F. Stögbauer. 2005. Effects of universal mobile telecommunications system (UMTS) electromagnetic fields on the blood-brain barrier in vitro. *Radiat. Res.* 164:258–269.

43. Zhou, J. X., G. R. Ding, ..., G. Z. Guo. 2013. Detrimental effect of electromagnetic pulse exposure on permeability of in vitro blood-brain-barrier model. *Biomed. Environ. Sci.* 26:128–137.

44. Bettinger, C., J. Borenstein, and S. Tao. 2013. Microfluidic Cell Culture Systems. William Andrew Publishing, Oxford, Waltham, MA.

45. Neuži, P., S. Giselbrecht, ..., A. Manz. 2012. Revisiting lab-on-a-chip technology for drug discovery. *Nat. Rev. Drug Discov.* 11:620–632.

46. Booth, R., and H. Kim. 2012. Characterization of a microfluidic in vitro model of the blood-brain barrier (μBBB). *Lab Chip.* 12:1784–1792.

47. Griep, L. M., F. Wolbers, ..., A. van den Berg. 2013. BBB on chip: microfluidic platform to mechanically and biochemically modulate blood-brain barrier function. *Biomed. Microdevices.* 15:145–150.

48. Prabhakarpandian, B., M. C. Shen, ..., K. Pant. 2013. SyM-BBB: a microfluidic blood brain barrier model. *Lab Chip.* 13:1093–1101.

49. Achyuta, A. K. H., A. J. Conway, ..., S. S. Sundaram. 2013. A modular approach to create a neurovascular unit-on-a-chip. *Lab Chip.* 13:542–553.

50. Duffy, D. C., J. C. McDonald, ..., G. M. Whitesides. 1998. Rapid prototyping of microfluidic systems in poly (dimethylsiloxane). *Anal. Chem.* 70:4974–4984.

51. Gumbleton, M., and K. L. Audus. 2001. Progress and limitations in the use of in vitro cell cultures to serve as a permeability screen for the blood-brain barrier. *J. Pharm. Sci.* 90:1681–1698.

52. Sixou, S., and J. Teissié. 1993. Exogenous uptake and release of molecules by electroloaded cells: a digitized videomicroscopy study. *Bioelectrochem. Bioenerg.* 31:237–257.

53. Ivorra, A., and B. Rubinsky. 2007. In vivo electrical impedance measurements during and after electroporation of rat liver. *Bioelectrochemistry.* 70:287–295.

54. Valič, B., M. Golzio, ..., D. Miklavčič. 2003. Effect of electric field induced transmembrane potential on spheroidal cells: theory and experiment. *Eur. Biophys. J.* 32:519–528.

55. Susil, R., D. Šemrov, and D. Miklavčič. 1998. Electric field-induced transmembrane potential depends on cell density and organization. *Electromagn. Biol. Med.* 17:391–399.

56. Dermol, J., and D. Miklavčič. 2015. Mathematical models describing Chinese hamster ovary cell death due to electroporation in vitro. *J. Membr. Biol.* 248:865–881.

57. Pucihar, G., and D. Miklavčič. 2010. The influence of intracellular connections on the electric field induced membrane voltage and electroporation of cells in clusters. *In* World Congress on Medical Physics and Biomedical Engineering, September 7–12, 2009, Munich, Germany. Springer, New York. 74–77.

58. Dermol, J., and D. Miklavčič. 2014. Predicting electroporation of cells in an inhomogeneous electric field based on mathematical modeling and experimental CHO-cell permeabilization to propidium iodide determination. *Bioelectrochemistry.* 100:52–61.

59. Mir, L. M., J. Gehl, …, M. Marty. 2006. Standard operating procedures of the electrochemotherapy: instructions for the use of bleomycin or cisplatin administered either systemically or locally and electric pulses delivered by the Cliniporator by means of invasive or non-invasive electrodes. *Eur. J. Cancer.* 4:14–25.

60. Ding, G. R., L. B. Qiu, …, G. Z. Guo. 2010. EMP-induced alterations of tight junction protein expression and disruption of the blood-brain barrier. *Toxicol. Lett.* 196:154–160.